J. Fluid Mech. (2012), *vol.* 710, *pp.* 545–568.
doi:10.1017/jfm.2012.376 Printed in the United Kingdom

The critical layer in linear-shear boundary layers over acoustic linings

E.J. BRAMBLEY[1]†, M. DARAU[2] AND S.W. RIENSTRA[2]

[1]Department of Applied Mathematics and Theoretical Physics, University of Cambridge, Wilberforce Road, Cambridge, CB3 0WA, UK

[2]Department of Mathematics and Computer Science, Eindhoven University of Technology, PO Box 513, 5600 MB, Eindhoven, The Netherlands

(Received Received 22 September 2011; revised 20 July 2012; accepted 20 July 2012; first published online 31 August 2012)

Acoustics within mean flows are governed by the linearized Euler equations, which possess a singularity wherever the local mean flow velocity is equal to the phase speed of the disturbance. Such locations are termed critical layers, and are usually ignored when estimating the sound field, with their contribution assumed to be negligible. This paper studies fully both numerically and analytically a simple yet typical sheared ducted flow in order to investigate the influence of the critical layer, and shows that the neglect of critical layers is sometimes, but certainly not always, justified. The model is that of a linear-then-constant velocity profile with uniform density in a cylindrical duct, allowing exact Green's function solutions in terms of Bessel functions and Frobenius expansions. For sources outside the sheared flow, the contribution of the critical layer is found to decay algebraically along the duct as $O(1/x^4)$, where x is the distance downstream of the source. For sources within the sheared flow, the contribution from the critical layer is found to consist of a nonmodal disturbance of constant amplitude and a disturbance decaying algebraically as $O(1/x^3)$. For thin boundary layers, these disturbances trigger the inherent convective instability of the flow. Extra care is required for high frequencies as the critical layer can be neglected only in combination with a particular downstream pole. The advantages of Frobenius expansions over direct numerical calculation are also demonstrated, especially with regard to spurious modes around the critical layer.

Key words: Aeroacoustics, pipe flow boundary layer, critical layers.

1. Introduction

Critical layers arise in inviscid shear flows as a mathematical singularity of the linearized Euler equations at points where the phase velocity is equal to the local fluid velocity, and give rise to a complex logarithmic singularity in the spatial Fourier transform of the solution. This can be smoothed out by taking into account additional viscous or nonlinear terms in the neighbourhood of the singular point (see Maslowe 1986; Huerre 1980; Huerre & Scott 1980). However, one can avoid adding complexity to the problem by defining a proper branch cut for the complex logarithm (Campos & Serrão 1998) based on causality arguments, with the restriction that the spatial Fourier inversion contour in the wavenumber plane should not cross the branch cut.

† Email address for correspondence: E.J.Brambley@damtp.cam.ac.uk

Critical layer singularities are associated with the continuous (hydrodynamic) spectrum (Rayleigh 1896; Case 1960), and have so far been demonstrated to have an algebraic rather than exponential decay or growth rate along the duct, with swirling flows (Golubev & Atassi 1996; Tam & Auriault 1998; Heaton & Peake 2006; Campos & Serrão 2010) in general exhibiting algebraic growth. Thus far, the reference for critical layers in a duct carrying sheared flow is Swinbanks (1975), who considered the sound field in a two-dimensional duct carrying parallel sheared flow with arbitrary Dirichlet-Neumann boundary conditions. He found that his eigenfunction representation of the pressure field generated by a mass source broke down at the critical layer, with his normal modes no longer forming a complete basis, leading to an additional contribution from the continuous spectrum. This latter part is only present downstream and contributes, in the worst case scenario when the source is at the critical layer, a singularity consisting of a simple pole and a logarithmic branch point. Inverting the Fourier transform, Swinbanks predicted an algebraic decay of $O(1/x^3)$ for a point mass source and of $O(1/x)$ for a source of distributed nature (although it should be noted that Swinbanks' analysis is not valid for a linear velocity profile for which the second derivative is identically zero). However, recently Félix & Pagneux (2007) demonstrated numerically $O(1/x)$ decay for a point source in a two-dimensional hard-walled duct with a parabolic mean flow profile, suggesting that further analytic investigation is warranted.

When determining the sound field in a lined duct, the critical layer is either explicitly (e.g. Brooks & McAlpine 2007) or tacitly (e.g. Olivieri, McAlpine & Astley 2010) ignored in the majority of cases, assuming its contribution to the total field to be insignificant. Numerical methods detect the critical layer branch cut as a set of spurious eigenvalues clustered on the positive real-wavenumber axis (Vilenski & Rienstra 2007*b*; Boyer, Piot & Brazier 2011). It is our purpose here to investigate the effects of the critical layer for a simple model having as few parameters as possible (see (2.5) below), and understand the effects linked to it, as well as its various contributions to the total field. As a consequence, we also demonstrate the difficulty of using conventional numerical methods in the neighbourhood of the critical layer, and the ability of the Frobenius method to overcome these difficulties (in line with the findings of Campos & Kobayashi 2008).

This paper is a study of the field generated by a time-harmonic point mass source in a circular duct with a constant-then-linear mean flow and a constant density profile. This choice is justified in the beginning of §2 as the simplest possible scenario where a critical layer singularity occurs; a constant-then-linear mean flow is a reasonably common simplifying assumption in the planar case (see e.g. Jones 1977), although, as will be seen, the cylindrical geometry is an important inclusion here. The mathematical solution is developed in §2. Linearizing the compressible Euler equations and Fourier transforming results in a single second order radial equation for the pressure, known as the Pridmore-Brown (1958) equation. Solutions to the Pridmore-Brown equation are given in §2.1 in terms of Bessel functions for the constant flow and Frobenius series for the linear shear (Campos, Oliveira & Kobayashi 1999), thus having the necessary tools for constructing the Green's function for a point mass source in §2.2. When the source is located in the constant flow part, the Green's function has an equivalent expression to the one for uniform flow (Rienstra & Tester 2008), as expected. We analyse the contributions from the poles in §2.3, finding the usual modal poles and, for the case when the source is in the boundary layer, an additional nonmodal hydrodynamic pole on the branch cut (also found by Swinbanks 1975) with a contribution of constant amplitude. Asymptotics are also given in §2.3 that prove that far downstream the branch cut integral is algebraically decaying as $O(1/x^4)$ for a source in the uniform flow, or $O(1/x^3)$ plus the constant amplitude contribution from the nonmodal pole mentioned above for a source within the boundary layer. This

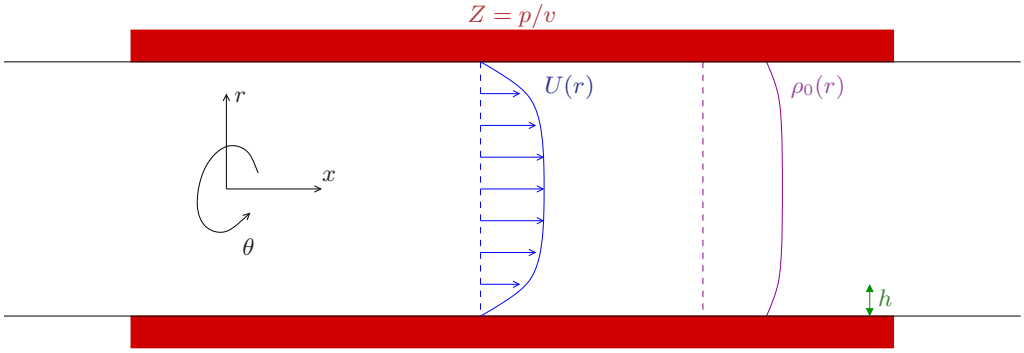

FIGURE 1. Schematic of sheared parallel flow in a cylinder with lined walls, with density $\rho_0(r)$, mean flow velocity $U(r)$, and boundary impedance Z.

analysis is then illustrated in §3 with a collection of numerical examples, demonstrating the field of the pole on the branch cut and a comparison with the uniform flow case. We also show here the effects of two additional modes linked to the critical layer: one that always has to be considered together with the branch cut, and the other a weak convective instability. In §3.7 the resolution of these modes by conventional numerical procedures is shown to be difficult due to many nearby spurious modes, while the Frobenius method employed here is shown to have no such difficulty.

2. Formulation of the mathematical problem

Consider an inviscid compressible parallel sheared flow within a cylinder with mean velocity $U(r)$ and density $\rho_0(r)$, as shown in figure 1. Time-harmonic acoustic perturbations to this flow of frequency ω can be found by Fourier series expansion in the circumferential coordinate θ and Fourier transformation to the axial coordinate x with wave number k. For suitable solutions $\tilde{p}(r;\, k, m)$ and amplitudes $A_m(k)$ the physical pressure field $p(x, r, \theta, t)$ is therefore given by the real part of the sum over Fourier integrals

$$p(x,r,\theta,t) = \mathrm{Re}\left(\frac{\mathrm{e}^{\mathrm{i}\omega t}}{2\pi} \sum_{m=-\infty}^{\infty} \mathrm{e}^{-\mathrm{i}m\theta} \int_{-\infty}^{\infty} A_m(k) \tilde{p}(r;\, k, m)\, \mathrm{e}^{-\mathrm{i}kx}\, \mathrm{d}k \right). \tag{2.1}$$

Well-chosen indentations of the k-inversion contour are understood when singularities of any kind along the real axis are to be avoided. In this paper we will be interested in a single m-mode, represented by the k-integral.

The resulting equation to be solved is known as the Pridmore-Brown (1958) equation, given in dimensional inhomogeneous form as

$$\tilde{p}'' + \Big(\frac{2kU'}{\omega - kU} + \frac{1}{r} - \frac{\rho_0'}{\rho_0} \Big) \tilde{p}' + \Big(\frac{(\omega - kU)^2}{c_0^2} - k^2 - \frac{m^2}{r^2} \Big) \tilde{p} = -\mathrm{i}(\omega - kU) \widetilde{S} \tag{2.2}$$

where the square of the speed of sound is $c_0^2 = \gamma p_0/\rho_0$ and the inhomogeneous forcing term $\widetilde{S}(r;\, k, m)$ is (the Fourier series and transform of) a mass source. This equation contains a regular singularity at $r = r_c$, where $\omega - kU(r_c) = 0$. This singularity is referred to as a critical layer singularity (with $r = r_c$ being the critical layer), and leads to a continuous hydrodynamic spectrum. Two linearly independent solutions to

the homogeneous problem $\widetilde{S} \equiv 0$ for $\tilde{p}$ expanded about r_c are

$$\tilde{p}_1(r) = (r-r_c)^3 + O\big((r-r_c)^4\big), \tag{2.3}$$

$$\tilde{p}_2(r) = A\tilde{p}_1(r)\log(r-r_c) + 1 - \tfrac{1}{2}(k^2 + m^2/r_c^2)(r-r_c)^2 + O\big((r-r_c)^4\big), \tag{2.4}$$

where

$$A = -\frac{1}{3}\left(k^2 + \frac{m^2}{r_c^2}\right)\left(\frac{U''(r_c)}{U'(r_c)} + \frac{\rho_0'(r_c)}{\rho_0(r_c)} - \frac{1}{r_c}\right) - \frac{2m^2}{3r_c^3}. \tag{2.5}$$

A relation similar to (2.5) regarding the existence of the critical layer is mentioned by Vilenski & Rienstra (2007*a*) for uniform density. The log-singularity is removed when the coefficient A is zero. In general, A will be nonzero, even for planar shear (rather than, as is considered here, cylindrical shear) where the $1/r_c$ and $2m^2/3r_c^3$ terms in (2.5) are not present. The notable case when A is identically zero is for linear planar shear of a uniform-density fluid. In other words, unless the shear is planar, the density is uniform, and the velocity is either constant or linear, then the log-singularity will in general be present. In this paper we will consider a linear shear with constant density in a cylindrical duct, which is the simplest possible scenario where a critical layer singularity occurs, with A nonzero owing to the non-planar shear due to the cylindrical geometry. In §2.1 we proceed to solve the homogeneous Pridmore-Brown equation (2.2) for this situation. This enables us to solve the inhomogeneous problem in §2.2, before inverting the Fourier transform to the get the spatial behaviour of $p(x,r)$ in §2.3.

2.1. *Solutions to the Pridmore-Brown equation*

We now consider a linear shear with constant density in a lined cylindrical duct with no slip along the duct walls, and scale distances on the duct radius a, velocities on the sound speed c_0, density on the mean density ρ_0, pressure on $\rho_0 c_0^2$ and wall impedance on $\rho_0 c_0$, thus having the duct wall at $r = 1$ and

$$U(r) = \begin{cases} M, & 0 \leqslant r \leqslant 1-h, \\ M(1-r)/h, & 1-h \leqslant r \leqslant 1, \end{cases} \tag{2.6}$$

with M the mean flow Mach number. Hence, the homogeneous form of (2.2) becomes

$$p'' + \Big(\frac{2kU'}{\omega - kU} + \frac{1}{r}\Big)p' + \Big((\omega - kU)^2 - k^2 - \frac{m^2}{r^2}\Big)p = 0, \tag{2.7}$$

subject to the boundary conditions that p is well behaved at $r = 0$ and that

$$\mathrm{i}Zp' - \omega p = 0 \qquad \text{at} \qquad r = 1, \tag{2.8}$$

where Z is the impedance of the lined duct walls. Since there is no slip at the duct walls, $U(1) = 0$, there is no need to resort to the Ingard–Myers boundary condition (Ingard 1959; Myers 1980) and the problem is wellposed (Brambley 2009; Rienstra & Darau 2011; Brambley 2011*b*). In order to solve (2.7) we consider separately the solution within the constant-flow region $r < 1 - h$ and the solution within the sheared region $r > 1 - h$.

2.1.1. *Solution within the constant-flow region*

The solutions to (2.7) are given within the uniform-flow section $r < 1 - h$ by

$$p = A\mathrm{J}_m(\alpha r) + B\mathrm{Y}_m(\alpha r) \quad \text{or equivalently} \quad p = C_1\mathrm{H}_m^{(1)}(\alpha r) + C_2\mathrm{H}_m^{(2)}(\alpha r), \tag{2.9}$$

where $\alpha^2 = (\omega - Mk)^2 - k^2$. Technically, since Bessel functions $\mathrm{Y}_m(z)$, $\mathrm{H}_m^{(1)}(z)$ and $\mathrm{H}_m^{(2)}(z)$ contain log-like singularities, a branch cut needs to be chosen for α, which (for fixed ω) leads to two branch cuts in the k-plane, here chosen as shown by the two dotted lines

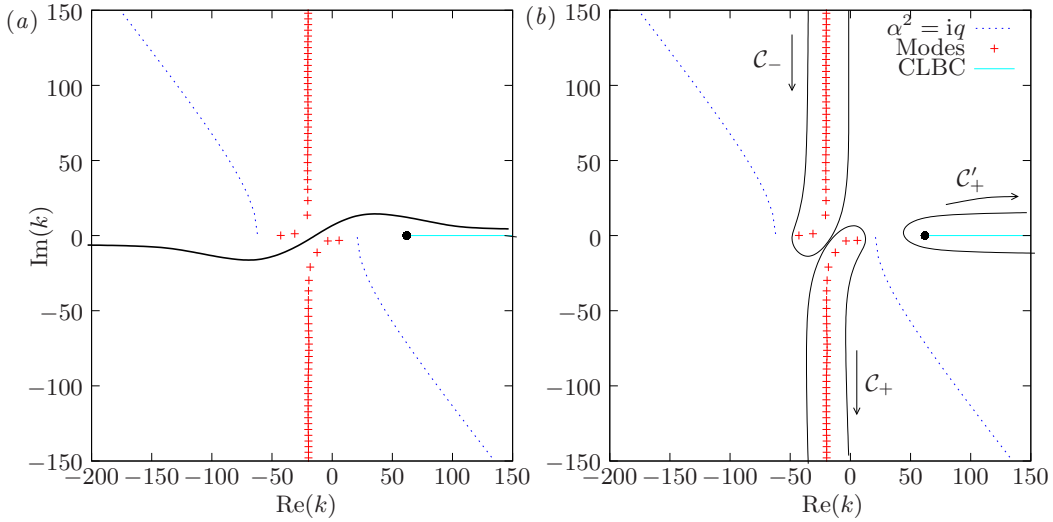

FIGURE 2. Schematic of the complex-k-plane, including branch cuts of α, the critical layer branch cut (CLBC), modes, and integration contours. (a) The undeformed causal inversion contour. (b) The inversion contour deformed for $x < 0$ ($\mathcal{C}_-$) and $x > 0$ ($\mathcal{C}_+$ and $\mathcal{C}'_+$).

in figure 2(a). However, these branch cuts turn out to be removable, at least as far as the Green's function is concerned. The integrals around these branch cuts are therefore identically zero, and so these branch cuts may be ignored as far as contour deformation is concerned (as shown in figure 2).

2.1.2. *Frobenius expansion for constant shear*

For $1-h < r < 1$, the mean flow becomes $U(r) = M(1-r)/h$ and the Pridmore-Brown equation is singular at $r = r_c$, where $r_c = 1 - \omega h/(kM)$, so that r_c is in general complex. Substituting $R = r - r_c$ into Eq. (2.7) for this constant shear gives

$$p_{RR} + \left(\frac{1}{r_c + R} - \frac{2}{R}\right)p_R + \left(\eta^2 R^2 - k^2 - \frac{m^2}{(R + r_c)^2}\right)p = 0, \tag{2.10}$$

where a subscript R denotes $\mathrm{d}/\mathrm{d}R$ and $\eta = Mk/h$. Following Campos *et al.* (1999), we pose a Frobenius expansion about this singularity, leading to the two linearly independent solutions:

$$p_1(r) = \sum_{n=0}^{\infty} a_n (r - r_c)^{n+3}, \tag{2.11a}$$

$$p_2(r) = \frac{1}{3r_c}\left(k^2 - \frac{m^2}{{r_c}^2}\right)p_1(r)\log(r - r_c) + \sum_{n=0}^{\infty} b_n (r - r_c)^n, \tag{2.11b}$$

$$a_n = \frac{1}{n(n+3)}\left[k^2 a_{n-2} - \eta^2 a_{n-4} - \sum_{q=0}^{n-1} a_{n-1-q}(-1)^q \big(n + 2 + (m^2 - 1)q\big)/{r_c}^{q+1}\right], \tag{2.11c}$$

$$b_n = \frac{1}{n(n-3)}\left[k^2 b_{n-2} - \eta^2 b_{n-4} - \sum_{q=0}^{n-1} b_{n-1-q}(-1)^q \big(n - 1 + (m^2 - 1)q\big)/{r_c}^{q+1}\right.$$
$$\left. - \frac{1}{3r_c}\left(k^2 - \frac{m^2}{{r_c}^2}\right)\left((2n-3)a_{n-3} + \sum_{q=0}^{n-4} a_{n-4-q}(-1)^q/{r_c}^{q+1}\right)\right], \tag{2.11d}$$

$$a_n = b_n = 0, \text{ for } n < 0; \quad a_0 = b_0 = 1; \quad b_3 = 0. \tag{2.12}$$

The branch cut for the log term in (2.11b) is taken away from the real-r-axis, so that $p_2(r)$ is a regular function of r for the physically relevant range $r \in [1-h, 1]$. For varying k, the direction of this branch cut therefore changes when the branch point at r_c crosses the interval $[1-h, 1]$ of the real r axis, leading to a branch cut in the k-plane on the real-k-axis for $k \in [\omega/M, \infty)$. It is this k branch cut that is referred to as the *critical layer branch cut*. For k below the critical layer branch cut, $\mathrm{Im}(r_c) < 0$, and for k above the critical layer branch cut, $\mathrm{Im}(r_c) > 0$. The change in $p_2(r)$ for k crossing the critical layer branch cut from below is therefore

$$\Delta p_2(r) = -\frac{2\pi\mathrm{i}}{3r_c}\left(k^2 - \frac{m^2}{{r_c}^2}\right)p_1(r)H(r_c - r), \tag{2.13}$$

where $H(r)$ is the Heaviside step function, while $p_1(r)$ remains continuous. We will also, on occasion, use the notation $p_2^{\pm}(r)$ to denote the solution $p_2(r)$ with the branch cut taken in the positive $(+)$ or negative $(-)$ imaginary-r directions, as these will be useful for analytic continuation.

2.2. *The Green's function solution*

Having found solutions to the homogeneous Pridmore-Brown equation (2.7), we now proceed to consider the inhomogeneous equation with point forcing (i.e. the Green's function), subject to impedance boundary conditions. Green's function solutions capture all possible physics of the problem, since any arbitrary driving disturbance or initial condition can be applied using them. In this paper we are only concerned with the point-mass-source Green's function; nonetheless, the results we obtain using this Green's function should be seen as, in some sense, general.

The field generated by a point mass source of unit strength located at $(x, \theta, r) = (0, 0, r_0)$, with $r_0 \neq 0$, is given by

$$G'' + \left(\frac{1}{r} + \frac{2kU'}{\omega - Uk}\right)G' + \left((\omega - Uk)^2 - k^2 - \frac{m^2}{r^2}\right)G = -\mathrm{i}(\omega - U(r_0)k)\frac{\delta(r - r_0)}{2\pi r_0}, \tag{2.14}$$

with the Green's function solution

$$G = \frac{-\mathrm{i}(\omega - U(r_0)k)}{2\pi r_0 \widetilde{W}(r_0; \psi_1, \psi_2)}\psi_1(r_<)\psi_2(r_>), \tag{2.15}$$

where $\widetilde{W} = \psi_1\psi_2' - \psi_1'\psi_2$, $r_< = \min\{r, r_0\}$, and $r_> = \max\{r, r_0\}$. The function ψ_1 is the solution to the homogeneous Pridmore-Brown equation (2.7) satisfying $\psi_1(0) = 0$ for $m \neq 0$ and $\psi_1'(0) = 0$ for $m = 0$. The function ψ_2 is a solution of the same equation, satisfying the impedance boundary condition (2.8). Both ψ_1 and ψ_2 are required to be C^1 continuous at $r = 1 - h$. We take

$$\psi_1 = \begin{cases} \mathrm{J}_m(\alpha r) & r \leqslant 1-h, \\ C_1 p_1(r) + D_1 p_2(r) & r \geqslant 1-h, \end{cases} \tag{2.16a}$$

$$\psi_2 = \begin{cases} A_2 \mathrm{H}_m^{(1)}(\alpha r) + B_2 \mathrm{H}_m^{(2)}(\alpha r) & r \leqslant 1-h, \\ C_2 p_1(r) + D_2 p_2(r) & r \geqslant 1-h. \end{cases} \tag{2.16b}$$

Bessel functions $\mathrm{H}_m^{(1)}$ and $\mathrm{H}_m^{(2)}$ are chosen for ψ_2, rather than the mathematically equivalent and more familiar J_m and Y_m, since the exponential behaviour of the Bessel functions is better handled numerically in this form (computed using the algorithm by Amos 1986). The coefficients A_2, B_2, C_1 and D_1 are chosen to give C^1 continuity at $r = 1-h$, and C_2 and D_2 are chosen to satisfy the boundary conditions (2.8) at $r = 1$, which for definiteness

we take to be $\psi_2(1) = 1$ and $\psi_2'(1) = -\mathrm{i}\omega/Z$. This eventually leads to

$$C_1 = \left.\frac{\mathrm{J}_m(\alpha r)p_2' - \alpha \mathrm{J}_m'(\alpha r)p_2}{W}\right|_{r=1-h} \qquad C_2 = \left.\frac{p_2' + \frac{\mathrm{i}\omega}{Z}p_2}{W}\right|_{r=1} \tag{2.17a}$$

$$D_1 = -\left.\frac{\mathrm{J}_m(\alpha r)p_1' - \alpha \mathrm{J}_m'(\alpha r)p_1}{W}\right|_{r=1-h} \qquad D_2 = -\left.\frac{p_1' + \frac{\mathrm{i}\omega}{Z}p_1}{W}\right|_{r=1} \tag{2.17b}$$

$$\begin{pmatrix} A_2 \\ B_2 \end{pmatrix} = \frac{\mathrm{i}\pi(1-h)}{4W(1)} \begin{pmatrix} \alpha \mathrm{H}_m^{(2)\prime} & -\mathrm{H}_m^{(2)} \\ -\alpha \mathrm{H}_m^{(1)\prime} & \mathrm{H}_m^{(1)} \end{pmatrix}_{r=1-h} \begin{pmatrix} p_1 & p_2 \\ p_1' & p_2' \end{pmatrix}_{r=1-h} \begin{pmatrix} p_2' & -p_2 \\ -p_1' & p_1 \end{pmatrix}_{r=1} \begin{pmatrix} 1 \\ -\mathrm{i}\omega/Z \end{pmatrix} \tag{2.17c}$$

where $W(r) = p_1(r)p_2'(r) - p_1'(r)p_2(r)$, so that $\widetilde{W}(r) = (C_1D_2 - C_2D_1)W(r)$, and the identity from Abramowitz & Stegun (1964) that the Wronskian $\mathcal{W}\big(\mathrm{H}_m^{(1)}(\alpha r), \mathrm{H}_m^{(2)}(\alpha r)\big) = -4\mathrm{i}/(\pi r)$ has been used for the final line. The function $W(r)$ may be calculated directly by substituting into (2.7), to give

$$W' + \left(\frac{1}{r} + \frac{2kU'}{\omega - Uk}\right)W = 0, \qquad \Rightarrow \qquad W(r) = -3\frac{r_c}{r}(r - r_c)^2, \tag{2.18}$$

where the multiplicative constant has been determined for the normalization of p_1 and p_2 used in (2.11a,b) by considering the limit $r \to r_c$.

We now consider the two cases of a source outside ($r_0 < 1-h$) and within ($r_0 > 1-h$) the sheared flow region separately, before ultimately combining them both into one expression.

2.2.1. *The Green's function for $r_0 < 1-h$*

In this case, the source is in the constant-flow region, so that $\psi_1(r_0)$ and $\psi_2(r_0)$ are given in terms of Bessel functions by (2.16*a*) and (2.16*b*). Expanding $\widetilde{W}(r_0; \psi_1, \psi_2)$ in (2.15) in this case and making further use of Bessel function identities from Abramowitz & Stegun (1964), we finally arrive at

$$G = \frac{-\mathrm{i}(\omega - Mk)W(1)}{2\pi(1-h)Q}\psi_1(r_<)\psi_2(r_>), \tag{2.19}$$

where $Q = W(1-h)W(1)\big(C_1D_2 - C_2D_1\big)$, so that

$$\begin{aligned} Q = {} & \big(\mathrm{J}_m(\alpha r)p_1' - \alpha \mathrm{J}_m'(\alpha r)p_1\big)\Big|_{r=1-h}\Big(p_2' + \frac{\mathrm{i}\omega}{Z}p_2\Big)\Big|_{r=1} \\ & - \big(\mathrm{J}_m(\alpha r)p_2' - \alpha \mathrm{J}_m'(\alpha r)p_2\big)\Big|_{r=1-h}\Big(p_1' + \frac{\mathrm{i}\omega}{Z}p_1\Big)\Big|_{r=1}. \end{aligned} \tag{2.20}$$

We note that outside the boundary layer (for $r < 1-h$) this may be written as

$$G(r) = -\tfrac{1}{4}\mathrm{i}(\omega - kM)J_m(\alpha r_<)\left[Y_m(\alpha r_>) - \frac{Y_m(\alpha(1-h)) - Z_1\alpha Y_m'(\alpha(1-h))}{J_m(\alpha(1-h)) - Z_1\alpha J_m'(\alpha(1-h))}J_m(\alpha r_>)\right] \tag{2.21}$$

$$Z_1 = \frac{\big[Zp_2'(1) + \mathrm{i}\omega p_2(1)\big]p_1(1-h) - \big[Zp_1'(1) + \mathrm{i}\omega p_1(1)\big]p_2(1-h)}{\big[Zp_2'(1) + \mathrm{i}\omega p_2(1)\big]p_1'(1-h) - \big[Zp_1'(1) + \mathrm{i}\omega p_1(1)\big]p_2'(1-h)}, \tag{2.22}$$

and we observe that by setting $h = 0$ we recover the Green's function for uniform flow obtained by Rienstra & Tester (2008).

2.2.2. *The Green's function for $r_0 > 1-h$*

If $r_0 > 1-h$, the Green's function source is located within the boundary layer. In this case, the Green's function is given by (2.15), with $\widetilde{W}(r_0;\psi_1,\psi_2) = (C_1D_2 - C_2D_1)W(r_0)$. Using (2.17*a*,*b*) and (2.18) gives

$$G = \frac{-\mathrm{i}(\omega - U(r_0)k)}{2\pi r_0}\frac{W(1)W(1-h)}{W(r_0)Q}\psi_1(r_<)\psi_2(r_>), \tag{2.23}$$

with Q as defined in (2.20).

2.2.3. *The Green's function for arbitrary r_0*

Note that the results in the previous two sections for $r_0 > 1-h$ and $r_0 < 1-h$ may be combined by defining $r^* = \max\{r_0, 1-h\}$ and setting

$$G = \frac{-\mathrm{i}\big(\omega - U(r^*)k\big)}{2\pi r^*}\frac{W(1)W(1-h)}{W(r^*)}\frac{\psi_1(r_<)\psi_2(r_>)}{Q}, \tag{2.24}$$

with Q being given by (2.20).

2.3. *Fourier inversion of the Green's function*

We now wish to invert the Fourier transform of the Green's function,

$$\tilde{G}(x,r,\theta,t;r_0) = \sum_{m=-\infty}^{\infty}\frac{1}{2\pi}\int_{-\infty}^{\infty} G(r;r_0,k,m)\,\mathrm{e}^{\mathrm{i}\omega t - \mathrm{i}kx - \mathrm{i}m\theta}\,\mathrm{d}k. \tag{2.25}$$

Here, we will be interested in a single m-mode, represented by the k-integral only.

2.3.1. *Choice of inversion contour*

The Fourier inversion contour in the k-plane must be chosen to satisfy causality, which we do here by applying the Briggs–Bers criterion (as in Rienstra & Darau 2011; Brambley 2011*b*). In summary, we consider $\mathrm{Im}(\omega)$ large and negative, for which G can be shown to be analytic in a strip $|\mathrm{Im}(k)| < \delta$ for some small $\delta > 0$. The Fourier inversion contour is taken within this strip (say along the real-k-axis), which guarantees causality. We then smoothly increase $\mathrm{Im}(\omega)$ to zero, and deform the k-inversion contour to maintain analyticity. The resulting k-inversion contour is shown in figure 2(*a*). For $x < 0$, the k-inversion contour may be closed in the upper half-plane, forming the inversion contour $\mathcal{C}_-$ shown in figure 2(*b*) that gives the contribution from the poles in the upper half-plane (the integral around the α branch cut being identically zero, as explained in section 2.2.1). For $x > 0$, the k-inversion contour similarly may be taken as $\mathcal{C}_+ \cup \mathcal{C}'_+$, with $\mathcal{C}_+$ giving the contribution from the poles in the lower half-plane and $\mathcal{C}'_+$ being the contribution from the critical layer branch cut. Note in particular that the Briggs–Bers analysis has specified that the critical layer branch cut is present only downstream of the point source, as expected. The Green's function solution $\tilde{G}$ will hence consist of a sum of residues of poles and an integral around the critical layer branch cut; the sum of residues of poles may be further separated into a sum over modal and nonmodal poles. These three cases are considered separately next.

2.3.2. *Contribution from modes*

Since the only poles of G come from zeros of the denominator of (2.24), there are two possibilities. If $Q = 0$ (implying that $C_1D_2 - C_2D_1 = 0$), then we have a mode in the normal sense, in that both ψ_1 and ψ_2 satisfy both boundary conditions at $r = 0$ and

$r = 1$. These poles' contribution to the Fourier integral is

$$R(k) = -\operatorname{sgn}(x)\frac{\omega - U(r^*)k}{2\pi r^*}\frac{W(1)W(1-h)}{W(r^*)}\frac{\psi_1(r_<)\psi_2(r_>)}{\partial Q/\partial k}\,\mathrm{e}^{-\mathrm{i}kx}\,. \tag{2.26}$$

The $\operatorname{sgn}(x)$ results from the direction in which the inversion contour goes around the pole. The only complication when considering the contribution of the modes is therefore to decide whether each mode occurs for $x < 0$ or $x > 0$, and this is answered by applying the Briggs–Bers criterion, as stated above. In general, modes with $\operatorname{Im}(k) > 0$ are stable and occur for $x < 0$, and modes with $\operatorname{Im}(k) < 0$ are stable and occur for $x > 0$, although, as will be seen later, there may exist an unstable mode with $\operatorname{Im}(k) > 0$ which should be counted as a mode for $x > 0$.

2.3.3. *Contribution from the k_0 nonmodal pole*

If the source is within the boundary layer, a second type of pole is possible for which $W(r_0) = 0$. Since p_1 and p_2 have been chosen to be linearly independent, this can only happen at a singular point of the Pridmore–Brown equation, i.e. when $r_0 = r_c$. At this point, we find

$$G(r; r_0) = \frac{\psi_1(r_<)\psi_2(r_>)}{C_1D_2 - C_2D_1}\left[\frac{-\mathrm{i}\omega k_0}{6\pi(1-r_0)^2 r_0}\left(\frac{1}{k-k_0} + \left(3 - \frac{1}{r_0}\right)\frac{1}{k_0} + O(k-k_0)\right)\right] \tag{2.27}$$

where $k_0 = \omega h/\big((1-r_0)M\big)$, so that there is a pole on the branch cut at $k = k_0$. It should be emphasized that this pole does not represent a mode, in that there is no solution to the Pridmore-Brown equation (2.7) that satisfies both boundary conditions at $r = 0$ and $r = 1$ with $k = k_0$, and indeed k_0 is a function of the point source position r_0, unlike the modes. Since k_0 is real, this contribution is of constant amplitude in x, and is found to only exist for $x > 0$. It corresponds physically to the trailing vorticity from the source (Rienstra, Darau & Brambley 2012), and exists only for a source within the sheared flow since a monopole will not shed vorticity in a uniform flow (a dipole being necessary to produce vorticity in uniform flow). The contribution from the k_0 pole is less than straightforward to calculate, since it is tied up with the integral around the critical layer branch cut, and indeed the residue of this pole is different if approached from above or below the branch cut. What will eventually be required is the contribution of this pole as if it were approached from above the branch cut, given by

$$P_+ = \lim_{q\to+0}\frac{-\omega k_0\,\mathrm{e}^{-\mathrm{i}k_0x}}{6\pi(1-r_0)^2r_0}\left(\frac{\psi_1(r_<)\psi_2(r_>)}{C_1D_2 - C_2D_1}\right)_{k=k_0+\mathrm{i}q}; \tag{2.28}$$

in effect, P_+ is calculated by substituting p_2^+ in place of p_2.

2.3.4. *Contribution from the critical layer branch cut and the k_- mode*

The integration contour we must use is shown in figure 3(a), and results in the branch cut contribution of

$$I = \frac{1}{2\pi}\int_{\omega/M}^{\infty}\big(G_+(r,k) - G_-(r,k)\big)\,\mathrm{e}^{-\mathrm{i}kx}\,\mathrm{d}k \tag{2.29}$$

where $G_+(r,k) = \lim_{\varepsilon\to0} G(r, k+\mathrm{i}\varepsilon)$ and $G_-(r,k) = \lim_{\varepsilon\to0} G(r, k-\mathrm{i}\varepsilon)$ denote the Green's function evaluated above and below the branch cut respectively. (In effect, $G_\pm$ is G with $p_2^\pm(r)$ taken in place of $p_2(r)$.) Progress may be made by deforming this contour of integration into the steepest-descent contour, as shown in figure 3(b). In deforming the contour, we must be careful not to allow the contour to cross any poles or branch points; figure 3 shows a k_- pole below the branch cut, a k_0 pole and branch point on the

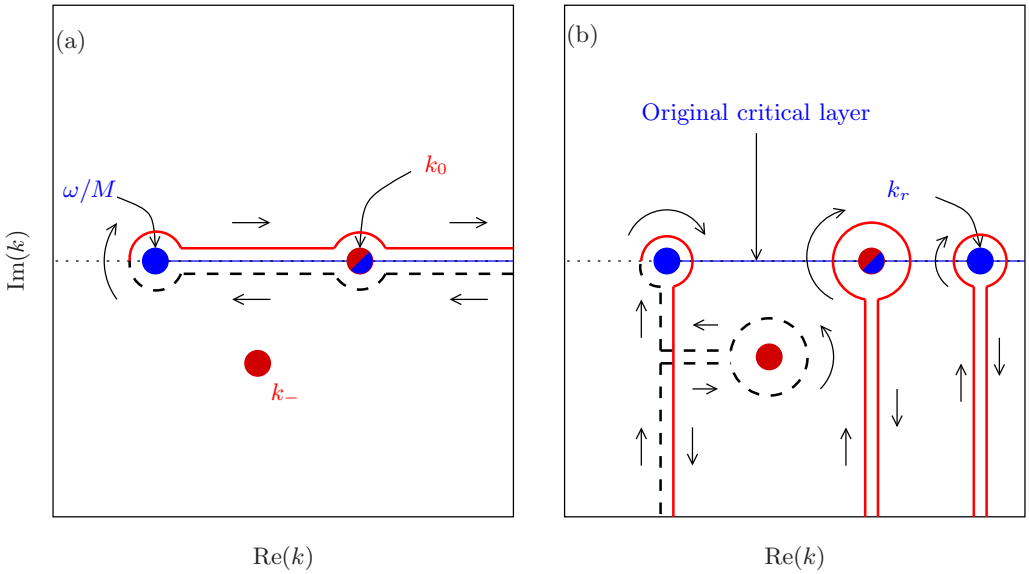

FIGURE 3. Schematic in the k-plane of the critical layer branch cut integral. Solid lines and dashed lines denote integrals of $G_+(k)$ and $G_-(k)$ respectively. a) The integral along the branch cut from the branch point (labelled ω/M) to infinity; and b) the same integral deformed onto the steepest-descent contour without crossing poles or branch points.

branch cut, and a k_r branch points on the branch cut, as will be justified later. Any k_- pole, being below the branch cut, is only a pole of G_- in (2.29). The pole contribution from integrating around this pole is therefore the negative of the pole contribution from k_- in the modal sum of all downstream-propagating modes, and the two exactly cancel. In effect, this deformation of the branch cut contour onto the steepest-descent contour removes any such k_- poles from the modal sum (we comment that, in §3, we find at most one such k_- pole). We hypothesise that there are no poles of G_+ that are crossed in this contour deformation, since such poles would necessarily lead to a discontinuous solution in r. We expect the integrals along the steepest-descent contour to be significantly smaller in magnitude than the integral along the critical layer branch cut; this expectation is formalized below.

For $r_0 > 1-h$, the integral I also contains a pole contribution from G_+ at $k = k_0$ as given in (2.28) above (note that k_0 is also a pole of G_- but it is only the pole from G_+ that contributes). As shown in the Appendix, we find there to be up to two branch points on the critical layer branch cut in addition to the one at ω/M, occuring at k_0 if $r_0 > 1-h$ and at $k_r \equiv \omega h/\big((1-r)M\big)$ if $r > 1-h$. This leads to up to three separate steepest-descent contributions, giving the critical layer branch cut contribution as

$$I = I_{\omega/M} + I_0 + I_r - P_+ - \sum_{k_-} R(k_-), \tag{2.30}$$

where

$$I_q = \frac{1}{2\pi\mathrm{i}} \int_0^\infty \Delta G_q(k_q - \mathrm{i}\xi)\, \mathrm{e}^{-\mathrm{i}(k_q - \mathrm{i}\xi)x}\, \mathrm{d}\xi, \tag{2.31}$$

with $k_{\omega/M} = \omega/M$, $\Delta G_{\omega/M}$, ΔG_0 and ΔG_r are given by (A 5), $\sum R(k_-)$ is the sum of the contributions from all k_- poles with $\mathrm{Re}(k_-) > \mathrm{Re}(\omega/M)$ and $\mathrm{Im}(k_-/\omega) < 0$, with $R(k)$ given in (2.26), and P_+ is the contribution from the pole at k_0 given by (2.28). (Note that (A 15) gives the effect on G_+ of the branch point at k_0 as being $O\big((k-k_0)^2\big)$, so that the presence of the branch point at k_0 does not change the P_+ contribution of

the pole at k_0.) For $r_0 < 1-h$ we take P_+ and I_0 to be zero, since in this case there is no pole or branch point at $k = k_0$, and similarly for $r < 1-h$ we take I_r to be zero.

In conclusion, the contribution from the integral around the branch cut together with any k_- poles below the branch cut consists of the P_+ pole contribution at k_0 (if $r_0 > 1-h$) and the steepest-descent contributions $I_{\omega/M}$, I_0 (if $r_0 > 1-h$) and I_r (if $r > 1-h$).

2.3.5. *Branch cut contribution for large x*

If some function $q(k)$ satisfies $q(K - \mathrm{i}\xi) \sim A\xi^\nu + O\big(\xi^{\nu+1}\big)$ to leading order for small ξ with $\nu > -1$, then Watson's lemma would give, in the large-x limit,

$$\frac{1}{2\pi\mathrm{i}} \int_0^\infty q(K - \mathrm{i}\xi)\, \mathrm{e}^{-\mathrm{i}(K-\mathrm{i}\xi)x}\, \mathrm{d}\xi \sim \frac{A\Gamma(\nu+1)\, \mathrm{e}^{-\mathrm{i}Kx}}{2\pi\mathrm{i}x^{\nu+1}} + O\big(1/x^{\nu+2}\big); \tag{2.32}$$

that is, an algebraically decaying wave convected with phase velocity ω/K. As shown in the Appendix (in A 11 and following A 15 and A 16) we find that, for the source in the main flow ($r_0 < 1-h$), $\Delta G_{\omega/M} \sim A_{\omega/M}\xi^3$, so that $I_{\omega/M}$ in the far field represents a wave convected with the uniform-flow velocity M and decaying algebraically as $O(1/x^4)$. Not only does this suggest a small contribution of $I_{\omega/M}$ to the total sound field, but we also find that, making suitable assumptions about the magnitudes of h being small and ω being large, the prefactor $A_{\omega/M} = O(h^2M^3/\omega^2)$, which is typically tiny. For the source within the boundary layer ($r_0 > 1-h$) we find $\Delta G_{\omega/M} \sim A_{\omega/M}\xi^4$, so that the decay of $I_{\omega/M}$ in this case follows an even higher rate of $O(1/x^5)$, with an even smaller prefactor $A_{\omega/M} = O(h^2M^4/\omega^3)$. These asymptotic predictions will be verified by comparison with numerical results in section 3. Similar predictions from appendix A.2 show that I_0 represents a wave convected with the flow speed at the source, $U(r_0)$, and decaying as $O(1/x^3)$ with a prefactor $A_0 = O(\omega h^3)$, while I_r represents a wave convected with the flow speed at the observer, $U(r)$, and decaying as $O(1/x^4)$ with a prefactor $A_r = O(Mh^3)$.

Although the predicted algebraic decay agrees with that predicted by Swinbanks (1975) in the case he analysed, $r_0 > 1-h$, it should be noted that Swinbanks investigated the two-dimensional case, and that his analysis is not valid for linear shear for which $U''(r) \equiv 0$; indeed (2.5) shows that, without the cylindrical curvature effect present here, a nonzero U'' is needed to give rise to a critical layer branch cut.

3. Numerical results

In this section, a number of illustrative numerical results are presented using the analysis above. Throughout this section we have taken a mean-flow Mach number $M = 0.5$ and an impedance of resistance $\mathrm{Re}(Z) = 2$. Whenever relevant, we have investigated stability by a Briggs–Bers analysis (as described by Rienstra & Darau 2011 and Brambley 2011*b*), with a simple impedance model of Helmholtz Resonator type (Rienstra 2006). For the numerical results that follow, all poles with $\mathrm{Im}(k) < 400$ were included in the sum of acoustic modes. This converged rapidly for $x \neq 0$, although the number of poles was insufficient to determine the solution at $x = 0$, as shown by the oscillatory radial behaviour at $x = 0$ in what follows. However, the advantage of this residue summation method is that the sum converges rapidly for large x, while direct numerical integration becomes problematic for large x owing to rapid oscillations of the integrand along the contour. The branch cut integrals were evaluated using a 4th-order-accurate direct numerical integrator on equally spaced points.

This section is organized as follows: in §3.1 we find the location of the poles referred to in §2.3, most of which correspond to duct modes. In §3.2 we compare the order

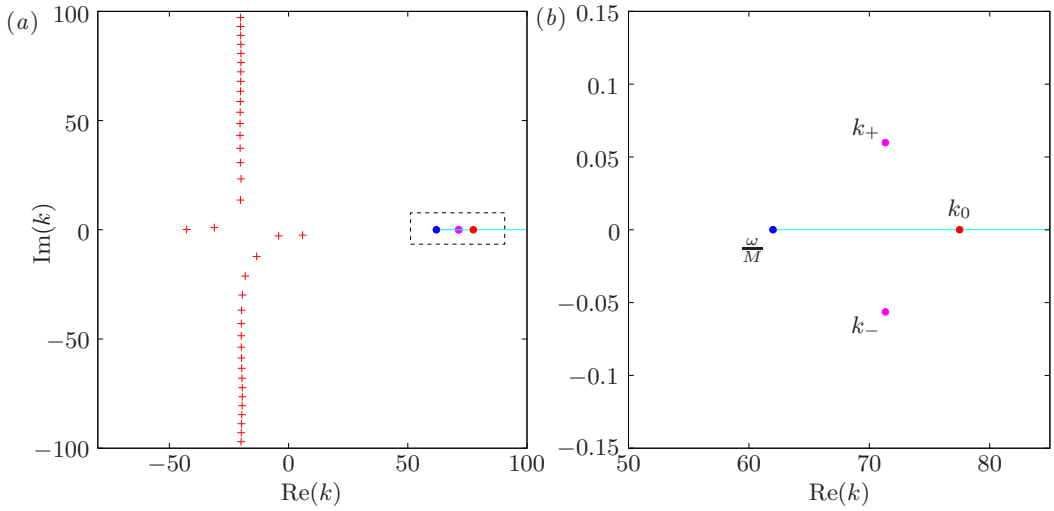

FIGURE 4. Overview of the k-plane: + acoustic poles; — branch cut; branch point ω/M, instability pole k_+, branch-cut-related pole k_- and neutrally stable pole k_0 (when the source location is in the boundary layer). (b) A zoom around the branch cut, approximately as indicated by the dashed rectangle in (a), although the height of the rectangle has been exaggerated. Poles as shown are for $\omega = 31$, $m = 24$, $M = 0.5$, $Z = 2 + \mathrm{i}$, $h = 0.05$, and $r_0 = 0.96$.

of magnitude of the acoustic modes to the k_+, k_-, k_0 and critical layer branch cut contributions. In §3.3 and §3.4 the effects of varying the boundary layer thickness h and the source location r_0 are investigated. In §3.5 the sheared flow solution is compared with what would have been obtained for uniform flow ($h \to 0$), while in §3.6 the accuracy of the asymptotics of §2.3.5 is verified against direct numerical calculation. Finally, in §3.7 the numerics based on the Frobenius method used here are compared with more traditional numerics.

3.1. *Location of poles*

Figure 4 shows a typical plot of the location of poles in the k-plane. In general, a downstream-propagating instability pole (denoted k_+) is always present in the upper half-k-plane just above the critical layer branch cut (corresponding to a surface mode of the sheared flow over the impedance boundary, Rienstra 2003; Brambley & Peake 2006; Brambley 2011*a*), and a maximum of a single k_- pole below the branch cut. The k_- pole is present for high frequencies, and crosses the branch cut to the other Riemann sheet for frequencies below a critical value (which depends on the impedance of the boundary and the thickness of the boundary layer). In addition to these, for $r_0 > 1 - h$ there is also the pole k_0 present on the branch cut.

3.2. *The magnitude of critical layer effects*

It is insightful to compare the order of magnitude of the contributions from the poles and the integral around the critical layer branch cut. Such a comparison is shown in figure 5. As can be seen from figure 5(*c*,*f*), the effects of the branch cut with k_0 pole subtracted (I') and the k_- mode appear important individually, and both are of the same order of magnitude as the instability (k_+). However, when the I' and k_- contributions are summed they almost totally cancel, with what remains being strongly localized about the mass source (figure 5*e*). This leads to an important observation: ignoring the critical layer but including the k_- pole in the modal sum produces serious errors in the total field. In conclusion, we can split the total pressure field into an acoustic part (obtained

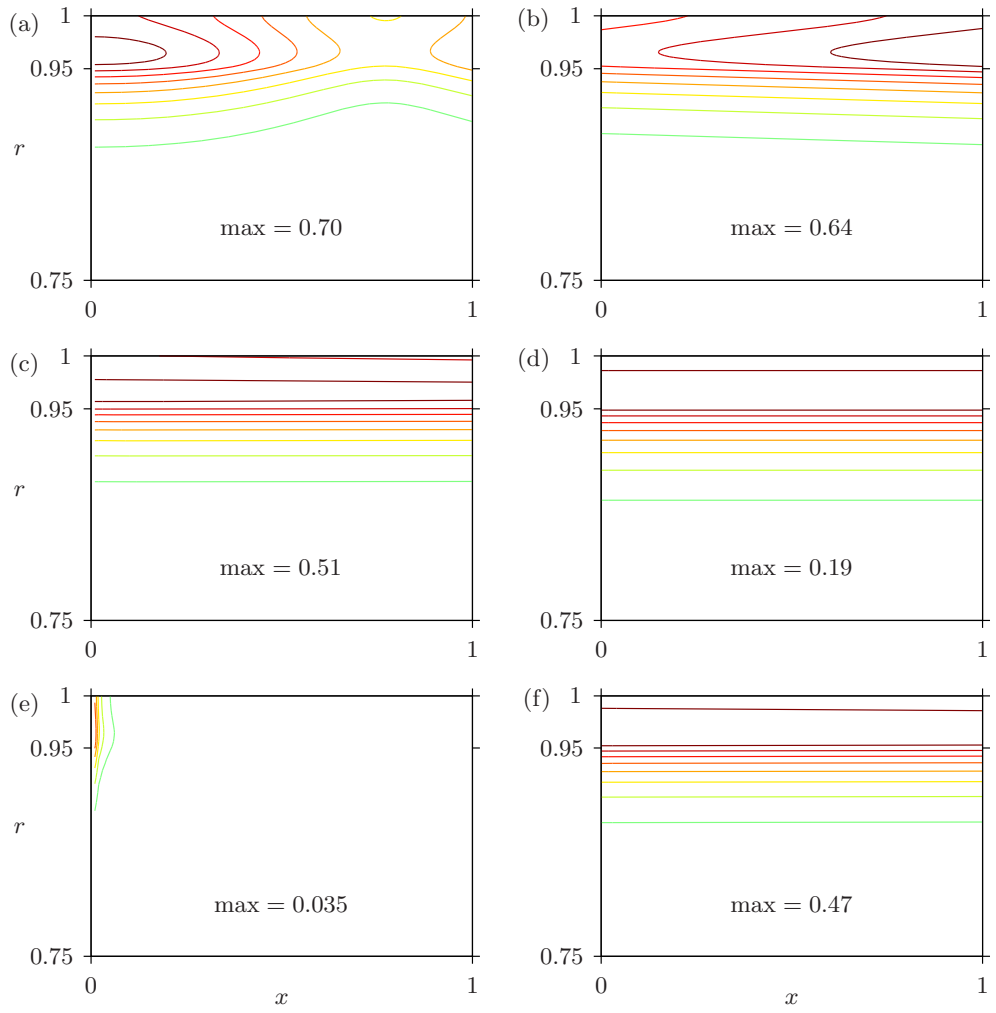

FIGURE 5. Comparison of the magnitude of different contributions to the Green's function from around the branch cut. Plots are of $|G(x,r)|$ on different scales, with contours spaced every 10% up to the maximum shown in each figure. (*a*) The integral around the branch cut (I, from equation 2.29); (*b*) the k_+ instability pole above the branch cut; (*c*) as (*a*) but with the k_0 pole on the branch cut subtracted; (*d*) the k_0 pole on the branch cut; (*e*) as (*b*) but with the k_- pole below the branch cut added; (*f*) the k_- pole below the branch cut. $Z = 2 + \mathrm{i}$, $\omega = 10$, $h = 0.05$, $M = 0.5$, $m = 2$, $r_0 = 0.96$.

by summing up the acoustic modes excluding any surface modes and k_-), a surface mode part (including the k_+ instability but excluding the k_- mode), the fields of the branch cut ($I_{\omega/M}$, I_0 and I_r), and the k_0 pole; note that the k_- mode never contributes, as its effect is incorporated into the branch cut's contribution. The k_0 contribution is only present if the source is in the boundary layer, and in this case the additional field generated by the k_0 pole (as shown in figure 6*b,ii*) may be interpreted as representing the hydrodynamic trailing vorticity wake caused by the presence of the source (Rienstra *et al.* 2012). Not too far downstream, we can see that for certain parameter values, the k_0 pole can have a contribution of the same order of magnitude as that of the instability pole k_+ (figure 5).

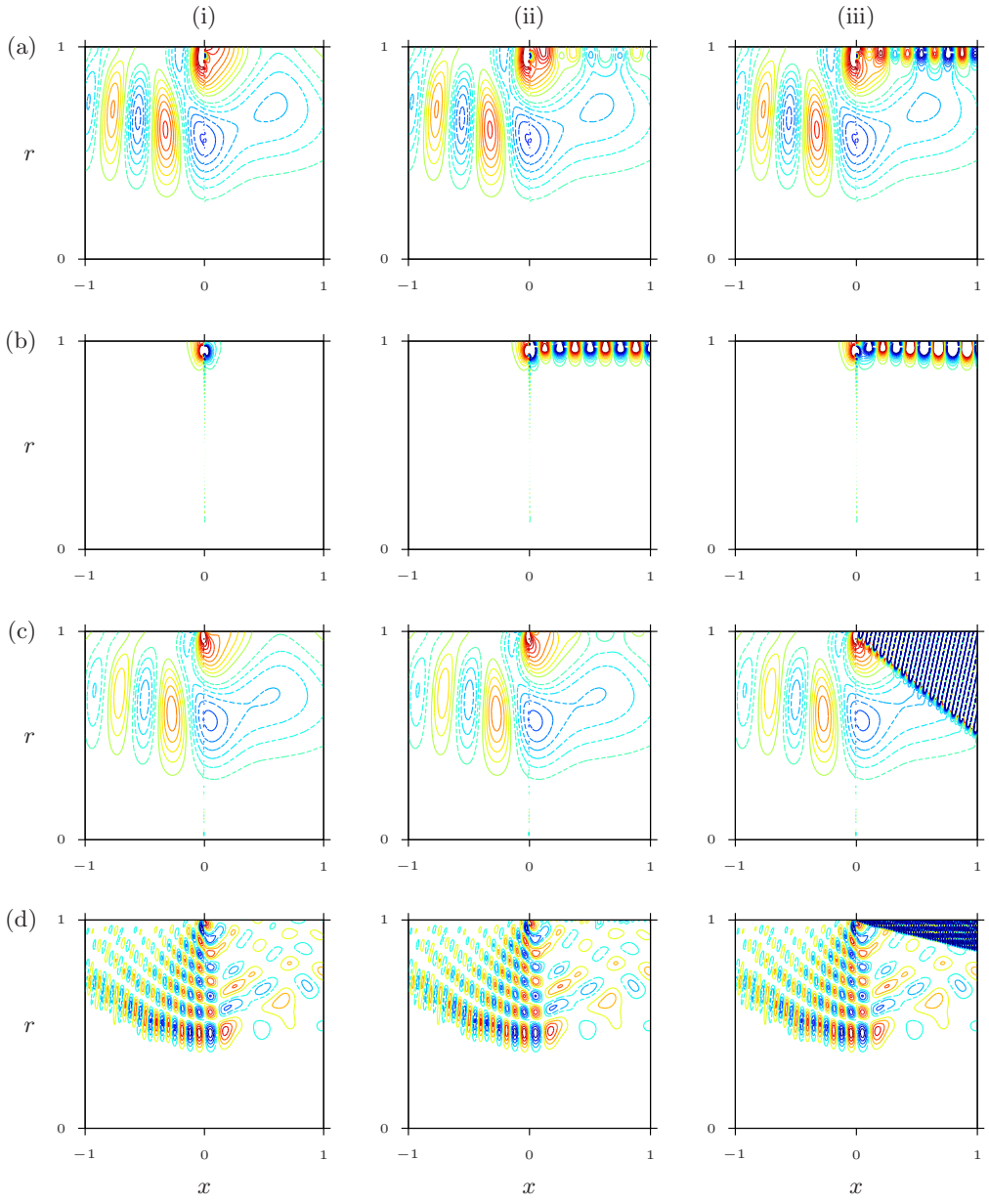

FIGURE 6. Contour plots of the pressure field in the (x, r)-plane. (i) sum of the acoustic poles; (ii) (i) plus the branch cut integrals and k_0 and k_- poles; (iii) all contributions. Hence, the only difference between (ii) and (iii) is the inclusion of the unstable k_+ mode. Solid lines indicate a positive pressure and dashed lines a negative pressure. $M = 0.5$ and $Z = 2 - \mathrm{i}$ for all plots; (a) $\omega = 10$, $m = 5$, $h = 0.05$, $r_0 = 0.96$; (b) $\omega = 10$, $m = 24$, $h = 0.05$, $r_0 = 0.96$; (c) $\omega = 10$, $m = 5$, $h = 0.001$, $r_0 = 0.9992$; (d) $\omega = 50$, $m = 24$, $h = 0.001$, $r_0 = 0.9992$.

3.3. *The effect of boundary layer thickness*

Figure 6 compares the influences of the critical layer and the instability mode k_+ to the acoustics for a point source within the boundary layer. Comparing figure 6(*a*,*b*)

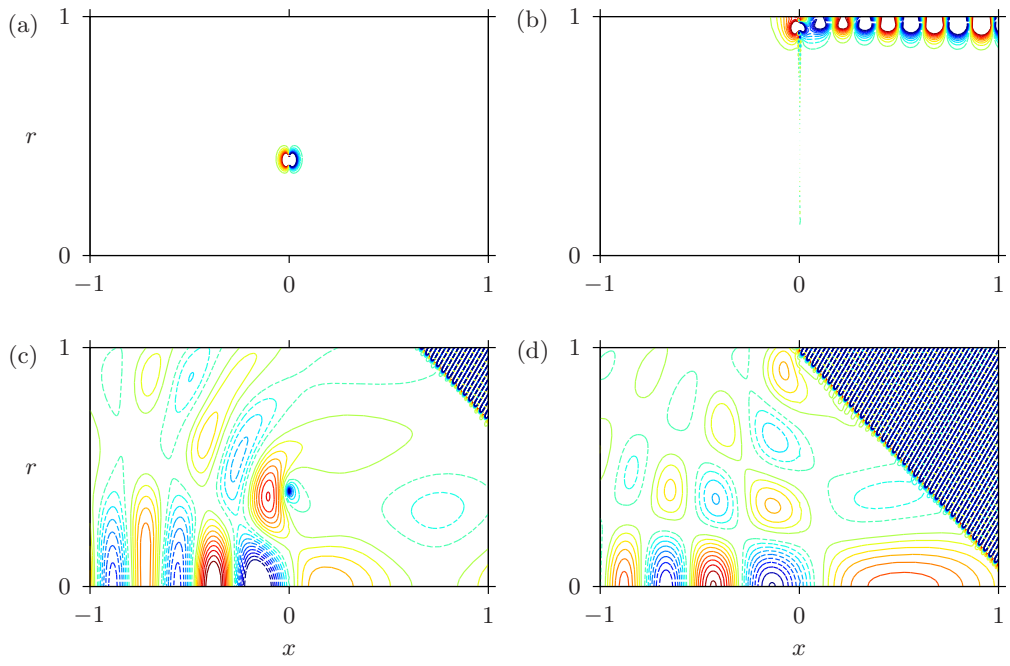

FIGURE 7. Total pressure field in the (x, r)-plane for (a)–(b) $\omega = 10$, $M = 0.5$, $m = 24$, $Z = 2-\mathrm{i}$, $h = 0.05$; (c)–(d) $\omega = 10$, $M = 0.5$, $m = 0$, $Z = 2+\mathrm{i}$, $h = 0.001$, and different source locations. Solid lines indicate a positive pressure and dashed lines a negative pressure. (a) $r_0 = 0.4$; (b) $r_0 = 0.96$; (c) $r_0 = 0.4$; (d) $r_0 = 0.9992$.

with 6(c,d) shows that as the boundary layer gets thinner, the severity of the instability pole k_+ gets stronger. In figure 6(c,d) the effect of the critical layer is noticeable and pervades into the duct significantly further than the boundary layer, although the effect is smaller in comparison to that of the k_+ instability. For thicker boundary layers (figure 6a,b), the effect of the critical layer is significant, and is even of comparable order to the k_+ instability in figure 6(b) for the range of x considered. Note that in figure 6(a,b) the k_+ instability is almost neutrally stable.

3.4. *The effect of the location of the point source*

We now compare the effect of a point source within ($r_0 > 1-h$) and outside ($r_0 < 1-h$) the boundary layer, with the significant difference that a source within the boundary layer leads to a k_0 pole contribution and I_0 branch cut contribution which are not present for the source outside the boundary layer. Figure 7 shows that for thicker boundary layers where the k_+ instability mode is not as strongly excited, the critical layer through the k_0 pole gives a significant difference between the source being within (figure 7b) and outside (figure 7a) the boundary layer. In contrast, if the boundary layer is thin enough that the k_+ instability dominates then the effect of placing the source within the boundary layer (figure 7d) is to trigger the instability earlier than had the source been placed outside the boundary layer (figure 7c), and the influence of the critical layer is minimal in this case.

It is clear from figures 6 and 7 that there is an instability mode present. For thicker boundary layers, this instability has a small growth rate (we remark that, in figure 6a, there is a growth in amplitude upon adding the residue k_+ (iii) to the field in (ii)). When

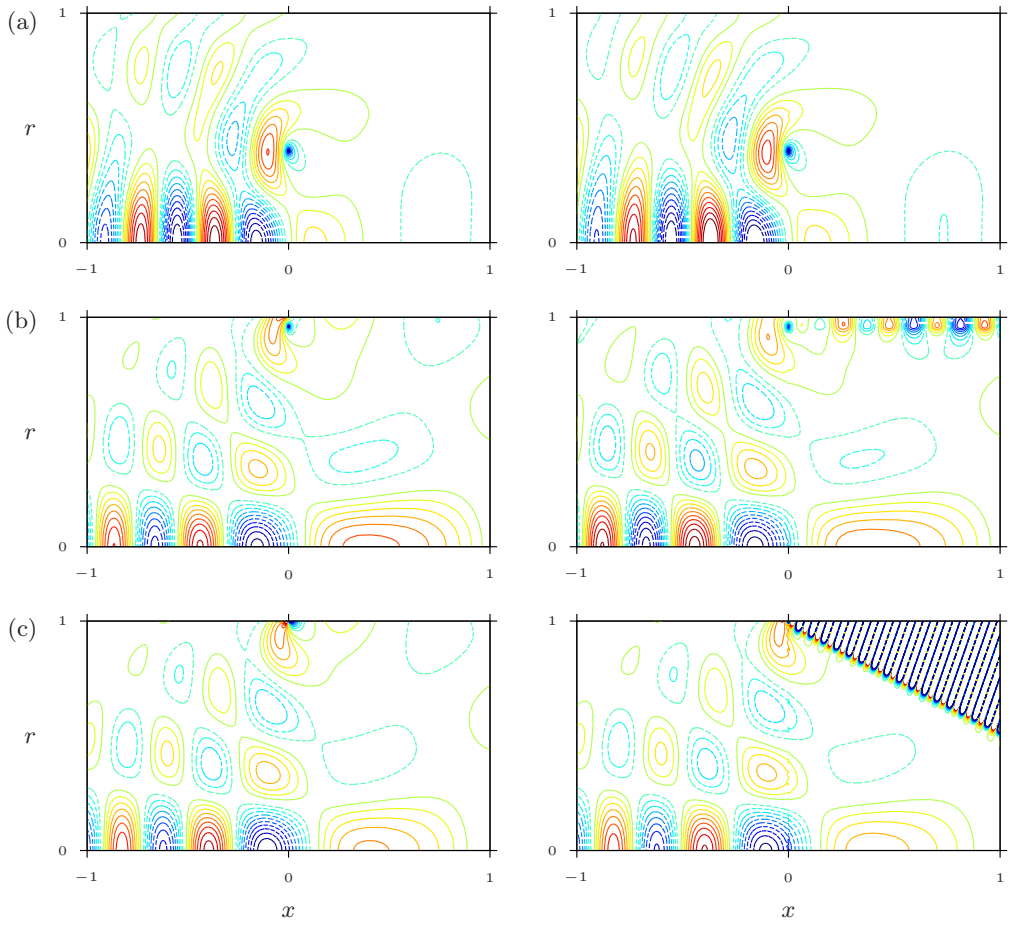

FIGURE 8. Contour plot in the (r, x)-plane of the Green's function with the source in the mean flow region for (left) a uniform flow with the Ingard–Myers condition, and (right) a constant-then-linear flow with boundary layer thickness h. Solid lines indicate a positive pressure and dashed lines a negative pressure. $\omega = 10$, $m = 0$, $M = 0.5$, and $Z = 2 - \mathrm{i}$: (a) $r_0 = 0.4$, $h = 0.05$; (b) $r_0 = 0.96$, $h = 0.05$; (c) $r_0 = 0.9992$, $h = 0.001$.

the source is in the boundary layer, the instability is immediately excited (figure 7*d*), as for a vortex-sheet Helmholtz instability from a trailing edge (Munt 1977; Rienstra 1981). When the source is outside the boundary layer, the excitation is moved further downstream (figure 7*c*), as for a free vortex sheet (Friedland & Pierce 1969; Jones & Morgan 1972).

3.5. *Comparison with uniform flow*

Figure 8 compares the response to a point source in uniform flow using the Ingard–Myers boundary condition (as found by Rienstra & Tester 2008 and given by (2.22) in the limit $h \to 0$) with the response to the same point source with a linear boundary layer. The critical layer is seen to be negligible when the source is in the mean flow (figure 8*a*), the pressure field being almost equivalent to that in a uniform flow. However, the critical layer is seen to become important when the source is in the boundary layer (figure 8*b,c*).

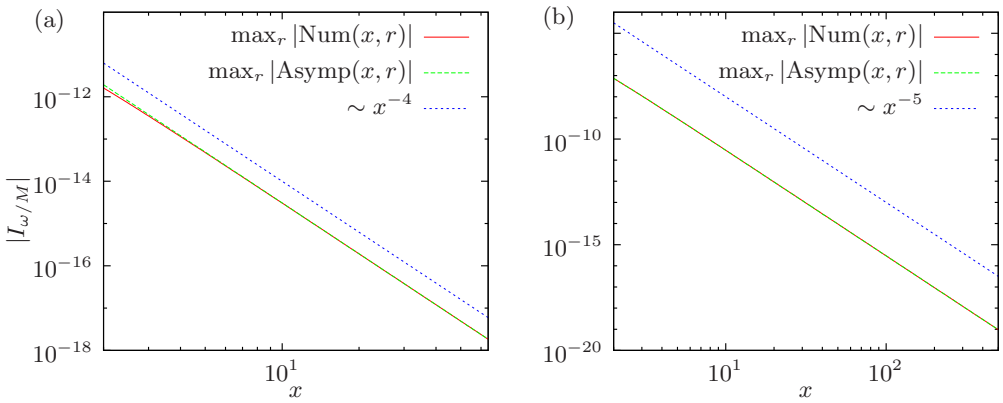

FIGURE 9. Comparison of the steepest-descent contour contribution from the $k = \omega/M$ branch point ($I_{\omega/M}$) calculated numerically ($\mathrm{Num}(x,r)$) and asymptotically ($\mathrm{Asymp}(x,r)$) using the asymptotics in the Appendix, for (a) the source in the main flow, $r_0 = 0.4$, and (b) the source in the sheared flow, $r_0 = 0.96$. The range of the x-axis is limited by the precision of the numerics. $\omega = 10$, $Z = 2 + \mathrm{i}$, $h = 0.05$, $m = 5$, and $M = 0.5$.

This is also demonstrated in figure 7(b), where all acoustic modes are cut off and the critical layer contribution is obviously dominant.

3.6. *Comparison of asymptotics and numerics*

The asymptotic predictions of algebraic decay of $I_{\omega/M}$, I_0 and I_r were verified by comparison with numerical results, of which only one example is shown here. Figure 9 shows the expected $O(1/x^4)$ and $O(1/x^5)$ decay of the steepest-descent branch cut contribution $I_{\omega/M}$ for the cases $r_0 < 1 - h$ and $r_0 > 1 - h$ respectively. The correctness of the leading-order coefficients in the Appendix was also verified numerically.

3.7. *Spurious modes on the critical layer branch cut*

From the analysis of §2, it is clear that the critical layer leads to a branch cut in the k-plane giving a contribution from deforming the Fourier inversion contour around it. This branch cut is also often referred to as a continuous spectrum, and many numerical procedures for calculating the modes of the Pridmore-Brown equation (2.7) find a large discrete number of spurious modes along this branch cut (e.g. Vilenski & Rienstra 2007*b*; Boyer *et al.* 2011), labelled as spurious as they do not in fact correspond to modal solutions of the Pridmore-Brown equation. One of the advantages of the Frobenius method described in (2.11) (following the work of Campos *et al.* 1999) is that it is particularly accurate near the branch cut (for which $r - r_c$ is small and the series converges quickly), and so does not suffer from numerical spurious modes (or other numerical inaccuracies, e.g., Campos & Kobayashi 2008). This is demonstrated in figure 10, which plots the modes calculated using a 12th order finite-difference solution of the Pridmore-Brown equation (the same program as used in Brambley 2011*a*,*b*) and the modes calculated using the Frobenius method, as has been used here. Figure 10(a) shows the acoustic modes to the left being well resolved by both methods, with the finite-difference method giving a large number of spurious modes along the critical layer branch cut. Figure 10(b) zooms in on these branch cut modes, and demonstrates that both methods also find the k_+ mode above the branch cut, although this mode might have been overlooked and accidentally classified as a spurious mode from only considering figure 10(a). More importantly, however, is figure 10(c) which zooms in on the branch cut even further and demonstrates

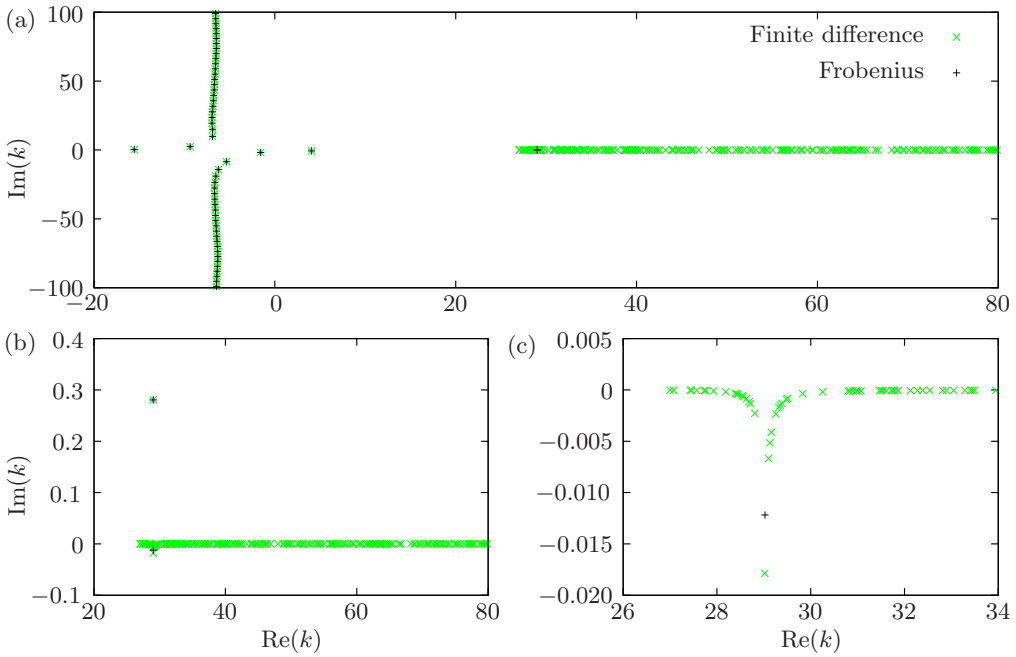

FIGURE 10. Comparison of axial wavenumbers of modes and spurious modes of the Pridmore-Brown equation (2.7) found using a 12th order finite-difference solution (×) to modes found using the Frobenius method of (2.11) (denoted +). (*a*) The acoustic and critical layer modes; (*b*) and (*c*) progressive zooms of the modes around the critical layer branch cut. $\omega = 10$, $m = 5$, $M = 0.5$, $h = 0.05$, and $Z = 2 + \mathrm{i}$.

that the finite-difference method, while influenced by the k_- pole below the branch cut, is unable to accurately predict its location, or even the number of such poles.

The clear advantage of the Frobenius method when compared with the finite-difference method is therefore that actual modes are not hidden within a mass of spurious modes about the critical layer branch cut, and that these modes are not only not hidden but are accurately computed; this advantage is expected to hold also when compared with other numerical methods, for example spectral methods. The disadvantage of the Frobenius method is that it is more difficult to apply to more general flow profiles other than the linear profile considered here, although some solutions for a few other simple flow profiles do exist (Campos & Serrão 1998; Campos & Kobayashi 2000, 2010; Campos & Oliveira 2011).

4. Conclusions

The Green's function for a mass source in a cylindrical duct with constant mean flow and a linear-shear boundary layer of thickness h has been given, this being the simplest case leading to a nontrivial critical layer; no restriction on h being either small or large has been assumed. The use of Frobenius series (motivated by Campos *et al.* 1999) to calculate the solution to the Pridmore-Brown equation (2.7) enables numerical solutions to be calculated which are particularly accurate around the critical layer branch cut and without the confusion of a large discrete number of spurious modes, as shown in figure 10. In sheared flow, there are three possible contributions to the pressure field: acoustic modes, surface modes (Rienstra 2003; Brambley & Peake 2006; Brambley 2011*a*), and

the critical layer branch cut (or, as it is sometimes called, the continuous spectrum). The first two occur as poles of the Green's function, the only difficult question in these cases being whether modes should be considered to be left-running (present for $x < 0$) or right-running (present for $x > 0$), which may be ascertained by applying the Briggs–Bers criterion (Rienstra & Darau 2011; Brambley 2011*b*). One of the aims of this paper was to address the third problem: that of the critical layer branch cut.

The critical layer branch cut (i.e. the continuous spectrum), through a Briggs–Bers analysis, is found to only take effect downstream of the point forcing and contributes in three ways:

(*a*) if the source is within the sheared flow region $r_0 > 1-h$, through the pole at $k = k_0$;
(*b*) through the integral along the branch cut, with the possible pole at k_0 removed; and
(*c*) through the pole just below or behind the branch cut (k_-).

The contributions from (*b*) and (*c*) are predicted to almost totally cancel and to decay algebraically away from $x = 0$. Note that either of critical layer effects (*b*) or (*c*) in isolation may give rather a large contribution (as seen in figure 5*c,f*), so that including the k_- pole below the branch cut but ignoring the branch cut itself would give significantly inaccurate results. The contribution from (*b*) and (*c*) together (i.e. the branch cut contribution excluding the possible pole at k_0) is here predicted asymptotically to decay as $O(1/x^4)$ and convect with the uniform-flow velocity M for a source in the uniform flow ($r_0 < 1-h$), and to decay as $O(1/x^3)$ and convect with the source's flow velocity $U(r_0)$ for a source in the boundary layer ($r_0 > 1-h$). While this agrees for $r_0 > 1-h$ with the $O(1/x^3)$ decay predicted by Swinbanks (1975), it should be noted that Swinbanks investigated the two-dimensional case, and that his analysis is not valid for linear shear for which $U''(r) \equiv 0$, so that different scalings would not have been unexpected. The scaling prediction of Swinbanks is unconfirmed numerically, especially since Félix & Pagneux (2007) demonstrated numerically $O(1/x)$ decay for a point source in a two-dimensional hard-walled duct with a parabolic mean flow profile, in apparent contradiction to the prediction of Swinbanks. Here, we can be confident about our predicted $O(1/x^4)$ and $O(1/x^3)$ decay since they are corroborated by direct numerical integration.

The dominant effect of the branch cut is due to the k_0 pole on the branch cut when it is present for $r_0 > 1-h$, which may in some cases dominate the effect of the instability mode k_+ for modest values of x (as seen in figure 6*b*). The instability mode k_+ is (in all cases considered here) a convectively unstable surface mode (Brambley 2011*a*) that dominates far downstream of the forcing point, while the k_0 pole on the branch cut (if present) is a nonmodal neutrally stable propagating disturbance with a phase velocity equal to the velocity of the mean flow at the point source $U(r_0)$. The field due to the k_0 pole may be interpreted as the trailing vorticity of the source (Rienstra *et al.* 2012). The physical manifestations of the k_+ and k_0 poles can be seen in figures 5(*b*) and 5(*d*) respectively, and also by comparing subfigures (i)–(iii) in figure 6. Whilst the analysis here has been for a duct with a lined wall, the same analysis is equally valid for a duct with a hard wall by taking the limit $Z \to \infty$; in this limit, both the k_+ and k_- modes are found to tend to finite values near to the critical layer, with the k_+ mode becoming neutrally stable, and the role of the k_0 pole remaining as described here.

A purely modal analysis of sheared flow would ignore the critical layer and any associated modes (including the k_- mode referred to above). The results presented here would seem to suggest that such an analysis should give good results provided there are no sound sources within any strongly sheared area of the flow and also provided that the k_+ unstable surface mode is included despite its proximity to the spurious modes around the critical layer (possibly with the aid of a surface mode approximation for sheared flow, Brambley 2011*a*). However, this is a generalization beyond the assumption of linear-

then-constant mean flow, while Félix & Pagneux (2007) appear to demonstrate different critical layer behaviour for a parabolic mean flow profile. Perhaps a more correct conclusion to draw from this work is that a linear-then-constant mean flow profile with sound sources only within the constant mean flow region is modelled well by a uniform-flow approximation with Ingard–Myers boundary condition provided the k_+ unstable surface mode is correctly predicted using a suitable shear-layer thickness (Brambley 2011*a*).

M.D.'s contribution was part of PhD work in a cooperation between TU Eindhoven (Netherlands) and the West University of Timişoara (Romania), supervised by Professors R.R.M. Mattheij and S. Balint. E.J.B. was supported by a Research Fellowship at Gonville & Caius College, Cambridge. A preliminary version of this work (Brambley, Darau & Rienstra 2011) was presented as part of AIAA paper 2011–2806 at the 17th AIAA/CEAS Aeroacoustics Conference, 6–8 June 2011, Portland, Oregon, USA.

Appendix A. Behaviour of ΔG

In this appendix we give details of the behaviour of $\Delta G \equiv G_+(r,k) - G_-(r,k)$, where $G_\pm$ are given by (2.24) with $p_2(r)$ substituted by $p_2^\pm(r)$ (as described following (2.11)). In what follows, all functions are to be evaluated as if below the branch cut in the k-plane (so p_2 implies p_2^-, etc), with $\Delta q = q^+ - q^-$ denoting the jump of any quantity across the branch cut from below to above.

First, note that for real $r_c > 1-h$ (i.e. for k on the critical layer branch cut),

$$\Delta p_2(r) = -\frac{2\pi\mathrm{i}}{3r_c}\left(k^2 - \frac{m^2}{{r_c}^2}\right)p_1(r)H(r_c - r), \quad \Delta p_2'(r) = -\frac{2\pi\mathrm{i}}{3r_c}\left(k^2 - \frac{m^2}{{r_c}^2}\right)p_1'(r)H(r_c - r), \tag{A 1}$$

so that $\Delta W = \Delta C_2 = \Delta D_2 = \Delta D_1 = 0$ and $\Delta C_1 = 2\pi\mathrm{i}D_1(k^2 - m^2/{r_c}^2)/(3r_c)$, and hence

$$\Delta\psi_1(r) = D_1\Delta\psi(r)H(r - r_c), \qquad \Delta\psi_2(r) = -D_2\Delta\psi(r)H(r_c - r), \tag{A 2}$$

where

$$\Delta\psi(r) = \begin{cases} \frac{2\pi\mathrm{i}}{3r_c}\left(k^2 - \frac{m^2}{{r_c}^2}\right)p_1(r) & r > 1-h \\ \frac{\pi^2(1-h)}{6r_c}\left(k^2 - \frac{m^2}{{r_c}^2}\right)\Big[\left(\alpha\mathrm{H}_m^{(1)\prime}p_1 - \mathrm{H}_m^{(1)}p_1'\right)_{r=1-h}\mathrm{H}_m^{(2)}(\alpha r) & \\ \qquad -\left(\alpha\mathrm{H}_m^{(2)\prime}p_1 - \mathrm{H}_m^{(2)}p_1'\right)_{r=1-h}\mathrm{H}_m^{(1)}(\alpha r)\Big] & r < 1-h. \end{cases} \tag{A 3}$$

From the definition of G (2.24),

$$G = \frac{-\mathrm{i}(\omega - U(r^*)k)}{2\pi r^* W(r^*)}\frac{\psi_1(r_<)\psi_2(r_>)}{C_1D_2 - C_2D_1}, \tag{A 4}$$

There are therefore three possible branch points of G in the k-plane: at $k = \omega/M$ where $r_c = 1-h$, and at each of $k = k_>$ and $k = k_<$, where $k_{<>} \equiv \omega h/\big(M(1 - r_{<>})\big)$ and hence $r_c = r_{<>}$. We may therefore write ΔG for real $k > \omega/M$ in three cases:

(i) For $r_< > 1-h$, using the identity $\Delta C_1D_2\psi_1 - (C_1D_2 - C_2D_1)D_1\Delta\psi = \Delta C_1D_1\psi_2$, we write

$$\Delta G = \frac{\mathrm{i}(\omega - U(r^*)k)}{2\pi r^* W(r^*)}\left[\frac{\Delta C_1D_1\psi_2(r_<)\psi_2(r_>)}{(C_1D_2 - C_2D_1 + \Delta C_1D_2)(C_1D_2 - C_2D_1)}\right. \\ \left. + \frac{D_1\Delta\psi(r_<)\psi_2(r_>)H(k-k_<)}{C_1D_2 - C_2D_1 + \Delta C_1D_2} + \frac{D_2\psi_1(r_<)\Delta\psi(r_>)H(k-k_>)}{C_1D_2 - C_2D_1 + \Delta C_1D_2}\right]. \tag{A 5a}$$

(ii) For $r_< < 1-h$ and $r_> > 1-h$, we write

$$\Delta G = \frac{\mathrm{i}(\omega - U(r^*)k)}{2\pi r^* W(r^*)}\left[\frac{\Delta C_1 D_2 \psi_1(r_<)\psi_2(r_>)}{(C_1D_2 - C_2D_1 + \Delta C_1 D_2)(C_1D_2 - C_2D_1)} + \frac{D_2\psi_1(r_<)\Delta\psi(r_>)H(k-k_>)}{C_1D_2 - C_2D_1 + \Delta C_1 D_2}\right]. \quad (\mathrm{A}\,5b)$$

(iii) For $r_> < 1-h$, we write

$$\Delta G = \frac{\mathrm{i}(\omega - U(r^*)k)}{2\pi r^* W(r^*)}\left[\frac{\Delta C_1 D_2 \psi_2(r_>) + (C_1D_2 - C_2D_1)D_2\Delta\psi(r_>)}{(C_1D_2 - C_2D_1 + \Delta C_1 D_2)(C_1D_2 - C_2D_1)}\psi_1(r_<)\right]. \quad (\mathrm{A}\,5c)$$

In what follows, we amalgamate these three cases as

$$\Delta G = \Delta G_{\omega/M} + \Delta G_0 H(k-k_0)H\big(r_0 - (1-h)\big) + \Delta G_r H(k-k_r)H\big(r-(1-h)\big), \quad (\mathrm{A}\,5d)$$

where $k_0 \equiv \omega h/(M(1-r_0))$ and $k_r \equiv \omega h/(M(1-r))$.

A.1. *Leading order behaviour of $\Delta G_{\omega/M}$ about $k = \omega/M$*

Here, we are interested in the behaviour of ΔG for $k = \omega/M - \mathrm{i}\xi$ in the limit $\xi \to +0$. Note that, in this case, $r_c \to 1-h$, so that

$$p_1(1-h) = \frac{-\mathrm{i}M^3h^3}{\omega^3}\xi^3 + O\big(\xi^4\big), \quad p_1'(1-h) = \frac{-3M^2h^2}{\omega^2}\xi^2 + O\big(\xi^3\big), \quad (\mathrm{A}\,6)$$

$$p_2(1-h) = 1 + O\big(\xi^2\big), \qquad p_2'(1-h) = \frac{-\mathrm{i}h\big(m^2M^2 + \omega^2(1-h)^2\big)\xi}{\omega M(1-h)^2} + O\big(\xi^2\big), \quad (\mathrm{A}\,7)$$

$$W(r) = \begin{cases} \dfrac{3M^2h^2}{\omega^2}\xi^2 + O\big(\xi^3\big) & r = 1-h \\ \dfrac{-3(1-h)}{r}\big(r-(1-h)\big)^2 + O(\xi) & r > 1-h \end{cases}. \quad (\mathrm{A}\,8)$$

We now substitute these into the formulae for the coefficients A_2, B_2, C_1, C_2, D_1 and D_2 from (2.17) and take the leading order terms in ξ. From these coefficients, we find that

$$C_1D_2 - C_2D_1 = \frac{-\mathrm{i}\omega^3 D_2 \mathrm{J}_m'\big(\mathrm{i}\omega(1-h)/M\big)}{3M^3h^2\xi^2} + O\big(1/\xi\big), \quad (\mathrm{A}\,9)$$

$$\Delta(C_1D_2 - C_2D_1) = \frac{-2\pi\mathrm{i}D_2\mathrm{J}_m\big(\mathrm{i}\omega(1-h)/M\big)}{3M^2(1-h)^3}\big(m^2M^2 - \omega^2(1-h)^2\big) + O(\xi). \quad (\mathrm{A}\,10)$$

Considering the four cases $r_0 \lessgtr 1-h$, $r \lessgtr 1-h$ separately, substituting the leading-order asymptotics discussed above and using Bessel function identities from Abramowitz & Stegun (1964) then leads to

$$\Delta G_{\omega/M} = \frac{\mathrm{i}M^3h^2\xi^3\big(m^2M^2 - \omega^2(1-h)^2\big)f(r)f(r_0)j(r_0)}{(1-h)^4\omega^4}\big(1 + O(\xi)\big), \quad (\mathrm{A}\,11)$$

where

$$f(r) = \begin{cases} \mathrm{I}_m(r\omega/M)/\mathrm{I}_m'\big((1-h)\omega/M\big) & r < 1-h \\ \dfrac{\mathrm{I}_m\big((1-h)\omega/M\big)}{\mathrm{I}_m'\big((1-h)\omega/M\big)}\left(p_2(r) - \dfrac{Zp_2'(1) + \mathrm{i}\omega p_2(1)}{Zp_1'(1) + \mathrm{i}\omega p_1(1)}p_1(r)\right) & r > 1-h \end{cases}, \quad (\mathrm{A}\,12)$$

$$j(r) = \begin{cases} 1 & r < 1-h \\ \dfrac{\mathrm{i}Mh\xi}{\omega\big(r-(1-h)\big)} & r > 1-h \end{cases}; \quad (\mathrm{A}\,13)$$

p_1 and p_2 are evaluated at $k = \omega/M$. We therefore derive the scalings (assuming ω is large and h is small, as is typical for acoustical applications)

$$\Delta G_{\omega/M} = \begin{cases} O\big(h^2M^3\xi^3/\omega^2\big) & r_0 < 1-h \\ O\big(h^2M^4\xi^4/\omega^3\big) & r_0 > 1-h \end{cases}. \tag{A 14}$$

The correctness of the $\Delta G_{\omega/M}$ asymptotics has been verified by comparison with numerical results.

A.2. *Leading order behaviour of $\Delta G_{<>}$ about $k = k_{<>}$*

In this section we investigate the behaviour of $\Delta G_>$ for $k = k_> - \mathrm{i}\xi$ and $\Delta G_<$ for $k = k_< - \mathrm{i}\xi$ in the limit $\xi \to +0$. Note that $\{k_<, k_>\} = \{k_r, k_0\}$. From (A 5) there are three cases to consider. Moreover, special care is required for the term $(\omega - U(r^*)k)/W(r^*)$ when expanding about k_0, since G contains a pole at $k = k_0$. After some algebra, we find that for $k = k_0 - \mathrm{i}\xi$, to leading order

$$\Delta G_0 \sim \frac{-(1-r_0)\xi^2\big(r_0^2\omega^2h^2 - (1-r_0)^2M^2m^2\big)}{9r_0^4\omega h^2\big((C_1+\Delta C_1)D_2 - C_2D_1\big)} \times \begin{cases} D_1\psi_2(r) & r > r_0 \\ D_2\psi_1(r) & r < r_0 \end{cases}, \tag{A 15}$$

with all coefficients evaluated at $k = k_0$. This gives $\Delta G_0 = O(\omega h^3\xi^2)$ at $k = k_0$. Note in particular that despite $G = O(1/\xi)$ due to the pole at $k = k_0$, $\Delta G_0 \to 0$ as $k \to k_0$, and hence the branch point at $k = k_0$ does not affect the pole contribution from G at $k = k_0$. For $k = k_r - \mathrm{i}\xi$, to leading order we find that

$$\Delta G_r \sim \frac{\mathrm{i}M(1-r)^3\xi^3\big(r^2\omega^2h^2 - (1-r)^2M^2m^2\big)}{9r^4\omega^2h^3(r-r_*)\big((C_1+\Delta C_1)D_2 - C_2D_1\big)} \times \begin{cases} D_1\psi_2(r_0) & r_0 > r \\ D_2\psi_1(r_0) & r_0 < r \end{cases}, \tag{A 16}$$

with all coefficients evaluated at $k = k_r$. This gives $\Delta G_r = O(Mh^3\xi^3)$ at $k = k_r$.

REFERENCES

Abramowitz, M. & Stegun, I. A. 1964 *Handbook of Mathematical Functions*, 9th edn. Dover.

Amos, D. E. 1986 Algorithm 644: A portable package for Bessel functions of a complex argument and nonnegative order. *ACM Trans. Math. Softw.* **12**, 265–273.

Boyer, G., Piot, E. & Brazier, J. P. 2011 Theoretical investigation of hydrodynamic surface mode in a lined duct with sheared flow and comparison with experiment. *J. Sound Vib.* **330**, 1793–1809.

Brambley, E. J. 2009 Fundamental problems with the model of uniform flow over acoustic linings. *J. Sound Vib.* **322**, 1026–1037.

Brambley, E. J. 2011*a* Surface modes in sheared flow using the modified Myers boundary condition. AIAA paper 2011-2736.

Brambley, E. J. 2011*b* A well-posed boundary condition for acoustic liners in straight ducts with flow. *AIAA J.* **49** (6), 1272–1282.

Brambley, E. J., Darau, M. & Rienstra, S. W. 2011 The critical layer in sheared flow. AIAA paper 2011-2806.

Brambley, E. J. & Peake, N. 2006 Classification of aeroacoustically relevant surface modes in cylindrical lined ducts. *Wave Motion* **43**, 301–310.

Brooks, C. J. & McAlpine, A. 2007 Sound transmission in ducts with sheared mean flow. AIAA paper 2007-3545.

Campos, L. M. B. C. & Kobayashi, M. H. 2000 On the reflection and transmission of sound in a thick shear layer. *J. Fluid Mech.* **424**, 303–326.

Campos, L. M. B. C. & Kobayashi, M. H. 2008 On the propagation of sound in a high-speed non-isothermal shear flow. *Int. J. Aeroacoustics* **8**, 199–230.

Campos, L. M. B. C. & Kobayashi, M. H. 2010 Sound transmission from a source outside a nonisothermal boundary layer. *AIAA J.* **48** (5), 878–892.

Campos, L. M. B. C. & Oliveira, J. M. G. S. 2011 On the acoustic modes in a duct containing a parabolic shear flow. *J. Sound Vib.* **330**, 1166–1195.

Campos, L. M. B. C., Oliveira, J. M. G. S. & Kobayashi, M. H. 1999 On sound propagation in a linear shear flow. *J. Sound Vib.* **219**, 739–770.

Campos, L. M. B. C. & Serrão, P. G. T. A. 1998 On the acoustics of an exponential boundary layer. *Phil. Trans. R. Soc. Lond.* A **356**, 2335–2378.

Campos, L. M. B. C. & Serrão, P. G. T. A. 2010 On the continuous spectrum of sound in sheared and swirling flows. AIAA paper 2010-4033.

Case, K. M. 1960 Stability of inviscid plane Couette flow. *Phys. Fluids* **3**, 143–148.

Félix, S. & Pagneux, V. 2007 Acoustic and hydrodynamic modes generated by a point source in a duct carrying a parallel shear flow. In *Proc. 19th International Congress on Acoustics, Madrid, 2–7 September*.

Friedland, A. B. & Pierce, A. D. 1969 Reflection of acoustic pulses from stable and instable interfaces between moving fluids. *Phys. Fluids* **12**, 1148–1159.

Golubev, V. V. & Atassi, H. M. 1996 Sound propagation in an annular duct with mean potential swirling flow. *J. Sound Vib.* **198**, 601–616.

Heaton, C. J. & Peake, N. 2006 Algebraic and exponential instability of inviscid swirling flow. *J. Fluid Mech.* **565**, 279–318.

Huerre, P. 1980 The nonlinear stability of a free shear layer in the viscous critical layer regime. *Phil. Trans. R. Soc. Lond.* A **293** (1408), 643–672.

Huerre, P. & Scott, J. F. 1980 Effects of critical layer structure on the nonlinear evolution of waves in free shear layers. *Proc. R. Soc. Lond.* A **371** (1747), 509–524.

Ingard, U. 1959 Influence of fluid motion past a plane boundary on sound reflection, absorption, and transmission. *J. Acoust. Soc. Am.* **31**, 1035–1036.

Jones, D. S. 1977 The scattering of sound by a simple shear layer. *Phil. Trans. R. Soc. Lond.* A **284**, 287–328.

Jones, D. S. & Morgan, J. D. 1972 The instability of a vortex sheet on a subsonic stream under acoustic radiation. *Proc. Camb. Phil. Soc.* **72**, 465–488.

Maslowe, S. A. 1986 Critical layers in shear flows. *Ann. Rev. Fluid Mech.* **18**, 405–432.

Munt, R. M. 1977 The interaction of sound with a subsonic jet issuing from a semi-infinite cylindrical pipe. *J. Fluid Mech.* **83**, 609–640.

Myers, M. K. 1980 On the acoustic boundary condition in the presence of flow. *J. Sound Vib.* **71**, 429–434.

Olivieri, O., McAlpine, A. & Astley, R. J. 2010 Determining the pressure modes at high frequencies in lined ducts with a shear flow. AIAA paper 2010-3944.

Pridmore-Brown, D. C. 1958 Sound propagation in a fluid flowing through an attenuating duct. *J. Fluid Mech.* **4**, 393–406.

Rayleigh, Lord 1896 *The Theory of Sound*, , vol. 2. Macmillan.

Rienstra, S. W. 1981 On the acoustical implications of vortex shedding from an exhaust pipe. *J. Engng Ind.* **103**, 378–384.

Rienstra, S. W. 2003 A classification of duct modes based on surface waves. *Wave Motion* **37**, 119–135.

Rienstra, S. W. 2006 Impedance models in time domain, including the extended Helmholtz resonator model. AIAA paper 2006-2686.

Rienstra, S. W. & Darau, M. 2011 Boundary-layer thickness effects of the hydrodynamic instability along an impednace wall. *J. Fluid Mech.* **671**, 559–573.

Rienstra, S. W., Darau, M. & Brambley, E. J. 2012 The trailing vorticity field behind a line source in 2D incompressible linear shear flow. *J. Fluid Mech.* (submitted).

Rienstra, S. W. & Tester, B. J. 2008 An analytic Green's function for a lined circular duct containing uniform mean flow. *J. Sound Vib.* **317**, 994–1016.

Swinbanks, M. A. 1975 The sound field generated by a source distribution in a long duct carrying sheared flow. *J. Sound Vib.* **40**, 51–76.

Tam, C. K. W. & Auriault, L. 1998 The wave modes in ducted swirling flows. *J. Fluid Mech.* **371**, 1–20.

Vilenski, G. G. & Rienstra, S. W. 2007*a* Numerical study of acoustic modes in ducted shear flow. *J. Sound Vib.* **307**, 610–626.

Vilenski, G. G. & Rienstra, S. W. 2007*b* On hydrodynamic and acoustic modes in a ducted shear flow with wall lining. *J. Fluid Mech.* **583**, 45–70.